Finite element simulations of the laser-heated diamond-anvil cell

Boris Kiefer[a)]
Physics Department, New Mexico State University, Las Cruces, New Maxico 88003

Thomas S. Duffy
Department of Geosciences, Princeton University, Princeton, New Jersey 08544

(Received 29 October 2004; accepted 18 March 2005; published online 24 May 2005)

Axial and radial temperature gradients in the laser-heated diamond-anvil cell are examined using finite element simulations. Calculations are carried out for an optically thin silicate or oxide sample separated from the diamonds by an insulation medium and heated by a TEM_{00} mode from an infrared laser. The peak temperature of the simulations was chosen to be a representative value (2200 K) and sample dimensions are typical for experiments in the 20–50-GPa range. The distance between the anvils is 30 μm. The total temperature drop across the sample in the axial direction is controlled by two parameters: the filling fraction (thickness of sample/distance between anvils) and the ratio of thermal conductivity between the sample and insulator (k_S/k_I). The results of the numerical calculations agree well with a one-dimensional numerical model. For a sample filling fraction of 0.5, the axial temperature drop will range from about 1000 K (>45%) for a thermal conductivity ratio of 1 to about 200 K (<10%) for a conductivity ratio of 10. If the conductivity ratio between sample and insulator is reduced to 1, then a sample filling fraction of less than 0.1 is required to keep the axial temperature decrease to be less than 10%. The effects of asymmetric samples and variations in absorption length are also examined. For a given gasket thickness and conductivity ratio, we find that radial gradients are minimal at a filling fraction of about 50% and then increase at higher and lower filling ratios. The anvil surface remains close to room temperature in all calculations. Our results demonstrate that reduction of axial temperature variations in optically thin laser-heated samples requires the use of thick, low thermal conductivity insulation media. © *2005 American Institute of Physics*. [DOI: 10.1063/1.1906292]

I. INTRODUCTION

The laser-heated diamond-anvil cell (LHDAC) has been a major tool for studying the static high-pressure and high-temperature properties of materials since its introduction in 1974.[1] An important feature of this device is that it can reach conditions exceeding even 100 GPa and 2500 K and thus is the only static device capable of investigating deep planetary interiors. In recent years, the LHDAC has been used to determine phase boundaries in silicates,[2–4] melting curves of metals and silicates,[5–9] melt structures at high *P-T*,[10] phase changes at ultrahigh pressure,[11–14] element partitioning,[15] and high-temperature equations of state.[16,17] In addition to these *in situ* experiments, laser heating is also widely used for high-pressure sample synthesis and relaxation of differential stress.

In the laser-heating technique, the sample is heated by an infrared laser while under compression in a diamond-anvil cell (DAC). Temperatures are measured by spectroradiometry.[18–21] The sample in a diamond-anvil cell is small, with typical dimensions of $\sim 10 \times 50$ μm^2. The small sample size together with the close proximity of the heat-absorbing diamond anvils means that strong axial and radial temperature gradients can develop in this device. These variations can create large uncertainty in measured temperatures.

The numerical calculations to simulate the temperature profile in LHDAC addressed the steady-state heat-flow problem under the assumption of constant thermal conductivity of all components and no insulating medium.[22] This work established that large temperature gradients are expected and made quantitative estimates of their magnitude. Such calculations show that heat flow is controlled radially by the shape and the dimension of the laser beam and axially by heat loss to the diamonds. A series of later studies further developed these results using semianalytical solutions to the heat-flow equation.[23–25] Finite element[26] and finite difference[27] simulations have also been used to investigate the temperature distribution, thermal pressure, equilibration time scales, and quench rates in the LHDAC.

In recent years, a number of experimental developments in laser-heating methods and accompanying analytical techniques have been adopted. For the sample assemblage, this includes the widespread use of insulation layers between the sample and diamonds[28] together with efforts to achieve thicker samples[29] and the double-sided hot-plate technique.[30] Improved heating techniques include the introduction of new laser types,[31] temperature control systems,[28,32,33] double-sided heating, and non-Gaussian laser modes.[33] Laser-heating systems have now been developed at synchrotron x-ray facilities for *in situ* high *P-T* diffraction and spectroscopy experiments.[33–37] A more recent series of semianalytical heat-flow calculations have examined some effects of changes in sample configuration on temperature gradients and the resulting x-ray diffraction patterns.[38–40]

[a)]Author to whom correspondence should be addressed; Electronic mail: bkiefer@nmsu.edu

In this paper, we examine the thermal structure of the laser-heated diamond-anvil cell by using finite element (FE) simulations. Previous FE simulations[26] have shown the usefulness of this technique but have examined only a narrow range of parameters. Here we expand this to include systematic study of the effect of variations in insulator thickness and thermal conductivity of sample and insulator. Numerical simulations are well suited to cope with the growing complexity of laser-heating experiments. More complex sample geometries can be readily incorporated in simulations, and pressure and temperature effects on material properties can be included, thereby reducing the number of approximations. Time-dependent calculations could also be carried out to gain insights into thermal evolution during laser-heated diamond-anvil cell experiments.

II. COMPUTATIONAL METHOD

Solutions to the heat-flow equation were obtained using the finite element software FLEX-PDE (3.03, PDE Solutions, Inc.). This program solves three-dimensional time-dependent partial differential equations including nonlinear and coupled systems. A particular feature of this software is automatic grid adjustment during program execution in order to resolve large gradients. We assume cylindrical symmetry of the diamond cell assembly and planar material boundaries perpendicular to the DAC axis. We neglect the effect of radiative heat transfer as this has been shown to be several orders of magnitude less efficient than diffusive heat transfer at peak temperatures of 2200 K.[18,25] We also neglect thermal equilibration times which are expected to be on the order of the thermal diffusion time scale, tens of milliseconds for typical sample sizes in LHDAC experiments.[27] This time scale is several orders of magnitude lower than the experimental time scale. Thus it is the long time (steady-state) solution of the heat equation that is relevant for the thermal structure in LHDAC experiments. The problem then reduces to the steady-state heat equation in cylindrical geometry

$$\frac{1}{r}\frac{\partial}{\partial r}k(T)r\frac{\partial T}{\partial r}+\frac{\partial}{\partial z}k(T)\frac{\partial T}{\partial z}=A(r,z), \tag{1}$$

where r, z, T, and $k(T)$ are the radial coordinate, vertical coordinate, temperature, and thermal conductivity, respectively, and $A(r,z)$ is the volumetric heating term that describes the interaction of the heating laser with the sample. Across all internal material boundaries the temperature and heat flow are assumed to be continuous. In addition, the temperature on the outermost limits of the simulation domain were set to ambient temperature.

The experimental geometry and computational grid are shown in Fig. 1 and material dimensions and properties are given in Table I. The heat-flow equation is solved for fixed volume. Depending on the detailed material parameters and DAC geometry, up to 3000 nodes were used in the simulations. A sufficient portion of the diamond anvils (85 μm) was included in the simulation domain in order to satisfy the room-temperature boundary condition along the outer boundary. We find that doubling the size of the included portion of the diamond and the gasket lead to negligible effects on the calculated thermal structure (less than 1 K).

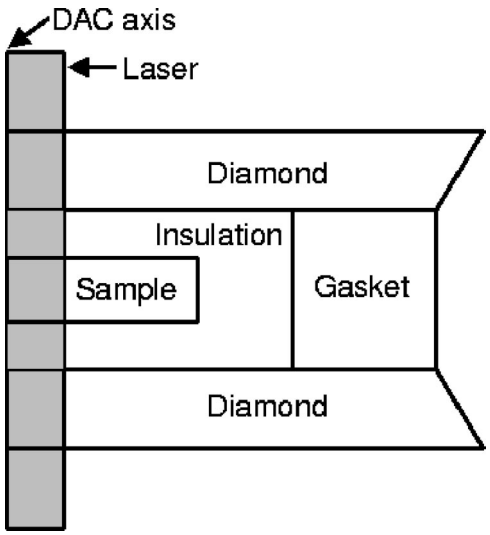

FIG. 1. Schematic illustration of showing a (r,z) slice through the simulation domain. The shaded region represents the radius of the laser beam. Typical dimensions and material parameters are specified in Table I.

All calculations were performed for optically thin samples and the optical absorption length was fixed at 200 μm, following Dewaele *et al.*[26] This approximation is justified by the measured optical absorption length (l) of dielectrics that is found to be in the range of $100-10^4$ μm,[22,41,42] usually much larger than the sample thickness (h_S). Therefore, the power density of the heating laser beam depends only on the radial distance from the DAC axis and is uniform along the axis of the sample. In this case, the volumetric heating rate of the laser that describes the source term in the heat equation [Eq. (1)] can be described as $A(r,z)=h_S Q(r)/l$. $Q(r)$ is the integrated power density of the laser, l is the optical absorption length, and h_S is the sample thickness. The power densities of the heating laser were modeled as TEM_{00} (gaussian) or TEM_{01} (donut) laser modes with radial power densities:[38]

$$Q(r,z)=Q_0 e^{-r^2/R^2}, \tag{2}$$

$$Q(r,z)=Q_0 r^2 e^{-r^2/R^2}. \tag{3}$$

For the TEM_{00} mode, R, the waist width of the laser beam is related to the full width at half maximum (FWHM) as $\mathrm{FWHM}=0.833\times R$. For TEM_{01}, R, is the separation of the maxima of the power density. The prefactor Q_0 is determined (iteratively) such that the maximum temperature in each

TABLE I. Typical model dimensions and input parameters.

Component	Material	Radius (μm)	Thickness (μm)	Thermal conductivity[a] (W/m K)
Sample	Silicate/oxide	30	3–30	2–20
Insulator	Argon, Al_2O_3	$\leqslant 50$	0–27	0.8–2; 45
Gasket	Steel	$50 \leqslant R \leqslant 150$	30	20
Anvil	Diamond	150	85	500

[a]Thermal conductivities at 300 K (for explantion see text).

simulation is 2200 K. The FWHM (20 μm) for the TEM_{00} mode was adopted from Dewaele *et al.*[26] It is also assumed that the insulation medium is completely transparent to the laser beam.

A significant advantage of this finite element approach is that the temperature dependence of material parameters can be readily incorporated. The temperature dependence of the thermal conductivity, k, is explicitly included here. In general, we have assumed that $k(T)=k(298)298/T$. The effect of different models for the temperature dependence of thermal conductivity is discussed below. We also neglect any anisotropy in thermal conductivity.

The anvil gap or gasket thickness was taken to be 30 μm. This is typical for laser-heating experiments at 20–50 GPa, a range of relevance for the Earth mantle phase boundary determination. The gasket hole diameter was assumed to be 100 μm, also typical for laser-heating experiments, but varying this parameter does not greatly affect the calculations. The varied parameters include the ratio of sample thickness (h_S) to gasket thickness (h_G) ("filling fraction") and the ratio of thermal conductivity of the sample to insulator. The latter was varied over the ranges given in Table I.

Our results below will demonstrate the importance of thermal conductivities of sample and insulator for determining thermal gradients in the diamond cell. Here we summarize the constraints on pressure and temperature dependence of k that are used to justify the ranges we have adopted for these quantities at the P-T range of interest. At ambient conditions, thermal conductivities generally range between 1–10 W/m K for typical silicates and oxides, with some exceptions such as Al_2O_3 (18–39 W/m K, Refs. 43–45) and MgO (33–55 W/m K, Refs. 43–46). These two exceptions are notable since both materials have sometimes been used as insulators in LHDAC experiments.[47,48] At ambient temperature, the thermal conductivity was extrapolated to 30 GPa using a linearized equation of state $k(P,300\ \mathrm{K})=k(0\ \mathrm{GPa},300\ \mathrm{K})[1+(K_0'/K_0)P]$, where $k(P,300\ \mathrm{K})$, $k(0\ \mathrm{GPa},300\ \mathrm{K})$, K_0', K_0, P are the thermal conductivity at pressure, thermal conductivity at ambient conditions, the zero pressure bulk modulus, its pressure derivative, and the pressure of interest, respectively.[43] The thermal conductivity of most oxides and silicates is in the range of 1–10 W/m K at ambient conditions.[43,44] Using the linearized equation of state we estimate that the thermal conductivity increases by 100%–200% for most oxides and silicates between 0 and 30 GPa. This suggests that their thermal conductivities at 30 GPa and room temperature may be in the range of 2–20 W/m K and we chose 8 W/m K as a representative value for the sample. Applying the same strategy to Al_2O_3 leads to 27–59 W/m K at 30 GPa and 300 K and we chose 45 W/m K as representative of a high thermal conductivity layer. For solid argon, experimental data up to only 100 K are available.[49,50] Assuming that the thermal conductivity (at constant pressure) between 10 and 100 K can be extrapolated to 300 K using $k\sim 1/T^{1.5}$ (Refs. 49–51) leads to a thermal conductivity of 0.015–0.027 W/m K at ambient conditions. The effect of compressions is estimated using the equation of state at ambient temperature, $K_0=3.03$ GPa and $K_0'=7.24$.[52] In contrast with oxides and silicates, the predicted thermal conductivity enhancement between 0 and 30 GPa is much higher due to the larger compressibility of argon. We obtain a factor of 70, leading to values of $k=0.8$–2 W/m K at 30 GPa and 300 K. A very recent theoretical study[53] shows that the thermal conductivity of argon at ambient temperature may be as high as 18 W/m K at 30 GPa. Thus the thermal conductivity of argon may approach or even exceed the thermal conductivity of the sample.

The temperature dependence of the thermal conductivity of the sample, the insulating medium, and the sample support (if present) was modeled as $k=k(300\ \mathrm{K})300/T$, appropriate for our simulations at constant volume.[54] While a variety of different forms for the pressure and temperature dependence of the thermal conductivity could be chosen, our results do not strongly depend on the particular model. At a given pressure, it is the ratio of sample to insulator thermal conductivity that will turn out to be the important parameter. Thus, the form of the temperature dependence of the conductivity is not a major factor if both sample and insulator have similiar temperature dependencies.

The high thermal conductivity of the diamonds and the gasket leads to comparatively low temperatures at their interfaces with the insulating medium. Therefore we chose the measured thermal conductivity of diamond at ambient conditions,[55] $k=500$ W/m K and neglect any pressure effect. This assumption is justified *a posteriori* from the modeling results. For the gasket we chose $k=20$ W/m K and neglected the temperature dependence for the same reason. While the physical properties of metals are variable, it is expected that the choice of the thermal conductivity of the gasket will not affect our results. The large separation of the gasket from the hotspot (50 μm) and the temperature across the insulator lead to comparatively low gasket temperatures. Therefore, the thermal conductivity of that gasket will be close to its value at ambient temperature.

III. RESULTS AND DISCUSSION

Figure 2 shows an example of a calculated temperature distribution in the laser-heated diamond cell. The laser beam profile was Gaussian with a FWHM of 20 μm. The sample geometry is the same as described previously except that the insulation medium below the sample is Al_2O_3 whereas that above and on the side of the sample is argon. In this simulation, the sample thickness (15 μm) is one-half of the gasket thickness (30 μm), corresponding to the 7.5-μm-thick insulation layers on each side. The sample/argon and sample/Al_2O_3 thermal conductivity ratios are 10 and 0.18, respectively. Despite identical insulation thicknesses, the axial thermal gradients on the top and bottom of the sample differ greatly due to the much higher thermal conductivity of the Al_2O_3 insulation layer. The axial temperature drop within the sample is 70 K on the argon side but reaches 1700 K on the Al_2O_3 side. However, the presence of the Al_2O_3 support affects temperatures throughout the sample as shown by the asymmetry of the radial and axial temperature contours (Fig. 2). Laser-heated samples are often probed using x-ray dif-

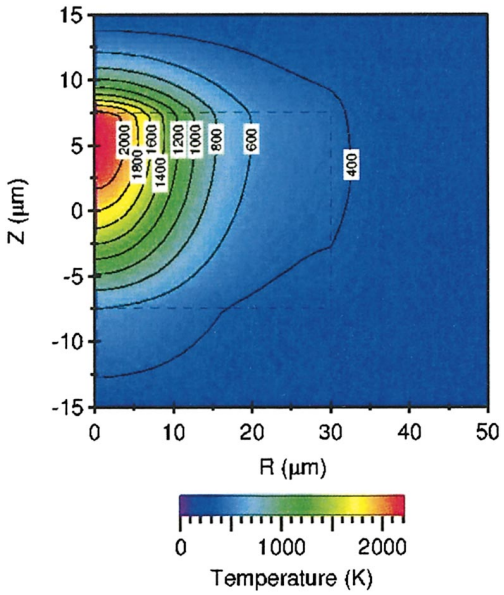

FIG. 2. (Color) The thermal structure calculated for 50% sample filling [$f=0.5$, see also Eq. (5)] when the sample rests on an Al_2O_3 support (below) with argon as an insulator above and on the side. The heating mode was a TEM_{00} with FWHM=10 μm. The sample consisted of an optically thin dielectric with a diameter of 60 μm, the gasket height was 30 μm, and the sample thickness was 15 μm.

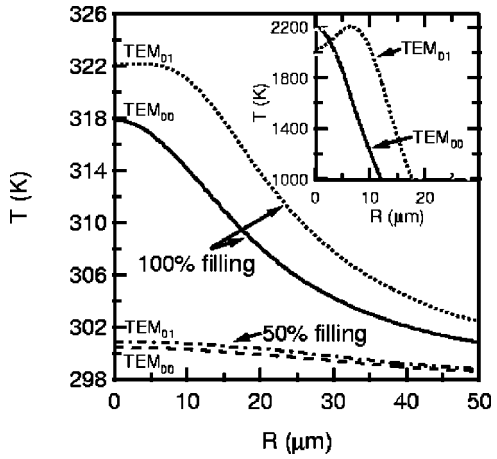

FIG. 3. Temperature distribution across the diamond culet interface for homogeneous heating. The FWHM was 20 μm for TEM_{00}. The peak separation of the TEM_{01} heating mode was 20 μm [see also Eq. (2)]. TEM_{00} mode: dashed line, 50% sample filling; Solid line, 100% sample filling. TEM_{01} mode: dot-dashed line, 50% sample filling; Dotted line: 100% sample filling. Inset: radial temperature distribution in the symmetry plane of the DAC ($z=0$). The lines have the same meaning as in the main figure.

fraction at synchrotron sources. The incident x-ray beam is typically about 10 μm in diameter and integrates along the sample thickness. In order to compare our results more directly with experiment, we calculated the average temperature in a cylinder of diameter 10 μm that is aligned with the DAC axis (and the laser beam) and extends through the length of the sample:

$$\overline{T} = 1/V \int_V T(r,z)dV, \tag{4}$$

where $\overline{T}$ is the volumetrically averaged temperature, V is the x-ray volume of the cylinder, and $T(r,z)$ is the temperature field obtained from the FE calculations. $\overline{T}$ corresponds to the average temperature in the regions sampled by a typical x-ray beam. For the above calculation, we find $\overline{T}=1480$ K, $\approx$33% lower than the 2200-K peak temperature in the calculation. These results highlight the importance of a low thermal conductivity of the insulation medium for minimizing axial temperature gradients. Furthermore this shows that significant differences may exist between the average temperature as sampled by x-rays compared with the radiometrically determined peak temperature.

We also investigated the temperature increase that occurs at the diamond/sample interface in simulations with and without an insulation medium (argon in this case) (Fig. 3). For a sample without any insulation, the anvil temperature increases slightly (to a maximum of 318 K) for a peak sample temperature of 2200 K. We also find that this result is unaffected by the heating mode of the laser. Using a TEM_{01} mode for heating results in almost the same temperatures (Fig. 3).

The filling ratio is defined as the ratio of sample thickness to gasket thickness:

$$f = h_S/h_G, \tag{5}$$

and describes the fraction of the total thickness between the anvils that is occupied by the sample. A filling fraction of $f=1$ means that there is no insulation layer whereas a filling fraction of $f \leqslant 0.5$ means that the total thickness of the insulation material equals or exceeds the thickness of the sample. For samples with appreciable amounts of insulation ($f \approx 0.5$), the anvil surface temperature increases by only a few degrees even directly above the central heating spot. These results justify our assumption that heat flow in the diamonds can be neglected.

In a previous numerical study using finite differences,[27] it was found that high anvil surface temperatures of 500–800 K resulted from laser heating with a Gaussian beam of ~25-μm waist and for gasket thicknesses between 15 and 45 μm. This finding is at variance with earlier numerical calculations that have reported that the anvils remain near room temperature.[22] Our calculations support the latter results, and the large temperatures of the earlier study[27] may be due to the low resolution of their numerical grid.

Axial and radial temperature gradients were calculated as a function of sample filling fraction for a case where the ratio of sample to insulator thermal conductivity at room temperature was fixed at $k_S/k_I=10$. As the filling fraction is decreased, the total axial temperature decrease across the sample is reduced [Fig. 4(a)]. The axial temperature gradient across the anvil gap for this symmetric assemblage always decreases from the maximum in the middle of the sample to near room temperature at the anvils. Thinner samples simply result in more of this temperature drop being achieved in the insulation layer.

We also find a nonmonotonic behavior of the curvature of the temperature at the center of the cell ($z=0$): As the sample thickness increases, initially a larger part of the sample remains at higher temperature up to an optimum thickness ($f \approx 0.5$, for $k_S/k_I=10$) and then the axial tempera-

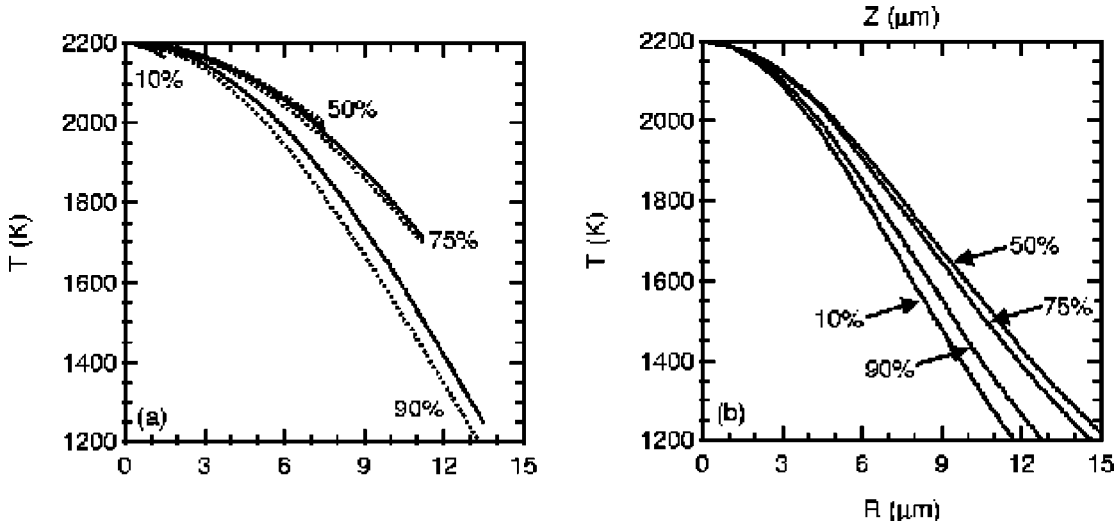

FIG. 4. The effect of sample filling ratio on the thermal structure in the LHDAC for a fixed thermal conductivity ratio, $k_S/k_I=10$. The sample was symmetrically centered in the diamond-anvil cell and had a diameter of 60 μm, the gasket thickness was fixed at 30 μm. The FWHM of the TEM_{00} heating was 20 μm. The labels next to the curves correspond to the filling fractions and to the actual sample thickness. (a) Axial temperature distribution. Solid lines: FE simulations; dotted lines: 1d analytical model. (b) Radial temperature distribution in the equatorial plane of the DAC. The inset shows the effect on sample filling on the FWHM. The radial edge is outside the graph at $R=30$ μm.

ture gradient increases again. This behavior can be rationalized by considering the radial (Q_R) and the axial (Q_Z) heat flow out of the hotspot (radius R_c) and out of the sample,

$$\frac{Q_R}{Q_Z}=\frac{h_S\Delta T_R/T_R}{R_c\Delta T_Z/T_Z}, \tag{6}$$

where ΔT_R, ΔT_Z, T_R, T_Z are the radial temperature change across the hotspot, the axial temperature change, the temperature on the radial edge of the hotspot, and the temperature at the sample/insulation boundary, respectively. The modeling shows that the radial temperature variation $\Delta T_R/T_R$ changes only little with sample filling. In contrast $\Delta T_Z/T_Z$ increases monotonically with increasing sample filling. Therefore, the optimum sample filling simply reflects the relative importance of axial and radial heat flow.

Radial temperature gradients as a function of filling fraction are shown in Fig. 4(b). Here we observe similar behavior as with the axial gradients. For larger sample filling fractions ($f\geqslant 50\%$, for $k_S/k_I=10$), the hotspot becomes narrower for thicker samples. For a peak temperature of 2200 K we find that the FWHM of the radial temperature profile between 50% and 90% sample filling decreases from 32.4 to 26.8 μm, a decrease of $\approx 17\%$.

To investigate this further, we developed a one-dimensional analytical model. The basic components of the model are continuity of temperature and heat flow across the sample/insulation medium interface, that the temperature drops to a reference temperature at the culet surface and that the peak temperature is reached in the center of the sample. The thermal conductivities in both sample and insulating medium were assumed to have the form $k_S=k_S(298\ \mathrm{K})298/T$ and $k_I=k_I(298\ \mathrm{K})298/T$, respectively. The coefficients $k_S(298\ \mathrm{K})$ and $k_I(298\ \mathrm{K})$ include the pressure effect on thermal conductivity. With these parameters the solution to the one-dimensional, steady-state heat-flow equation becomes

$$T(z)=\begin{cases} T_0\exp[4sY(z+h_G/2)/h_S] \\ \quad for\ -h_G/2\leqslant z\leqslant -h_S/2, \\ T_{\max}\exp\{-s[z/(h_S/2)]^2\} \\ \quad for\ -h_S/2\leqslant z\leqslant h_S/2, \\ T_0\exp[-4sY(z-h_G/2)/h_S] \\ \quad for\ h_S/2\leqslant z\leqslant h_G/2. \end{cases} \tag{7}$$

with

$$s=\frac{\ln(T_{\max}/T_0)}{1+2Y(1/f-1)}, \tag{8}$$

where $Y=k_S(298\ \mathrm{K})/k_I(298\ \mathrm{K})$ is the ratio the thermal conductivities of the sample and the insulator and $f=h_S/h_G$ is the sample filling ratio. $T_{\max}$, T_0, h_S, and h_G are the peak temperature, reference temperature on the culet, sample thickness, and gasket thickness, respectively. In Fig. 5 the results of the analytical model (solid lines) are compared with the FE simulations (solid symbols). Figure 5 shows that the axial temperature drop across the sample grows as the filling fraction increases. For a small thermal conductivity difference between the sample and the insulation, the temperature drop increases sublinearly with filling fraction (filled squares in Fig. 5). For the case of a large thermal conductivity contrast, the temperature drop increases only slowly up to sample fillings of $f\approx 0.75\%$ and then increases rapidly (filled circles in Fig. 5). The differences between the FE simulation and the one-dimensional (1D) analytical model at small sample fillings arise from the larger radial temperature gradients in this case [Fig. 5(b)] but never exceed 80 K [Figs. 4(a) and 5]. The analytical model and FE simulations show that the axial temperature drop across the sample depends strongly on both the conductivity ratio and the sample filling fraction. The axial temperature drop between the center of the sample and the sample/insulating

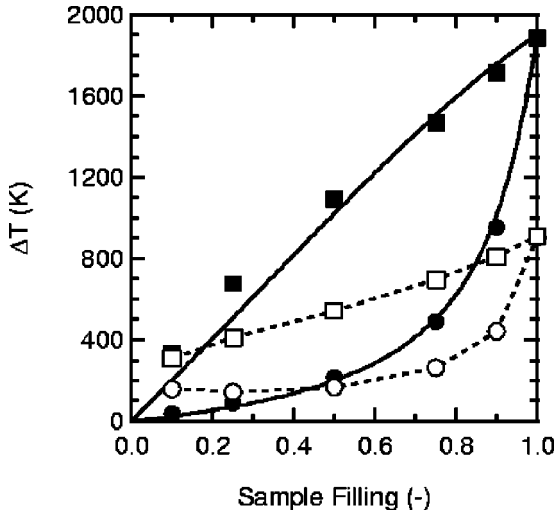

FIG. 5. Comparison of axial and radial temperature variations from FE simulations with the one-dimensional analytical model. The circles and squares refer to FE simulations with thermal conductivity ratios $[Y = k_S(298\ K)/k_I(298\ K)]$ of $Y=10$ and $Y=1.1$, respectively. The heating mode in the FE calculations was TEM_{00} with FWHM=10 μm. The filled symbols correspond to the axial temperature decrease between the center and the edge of the sample. The solid lines are the predictions from the one-dimensional analytical model. The open symbols correspond to the volumetrically averaged temperature decrease in a cylinder with a 10-μm diameter based on the FE results. This simulates the volume that would be sampled by an x-ray beam. The dashed lines are guides to the eye.

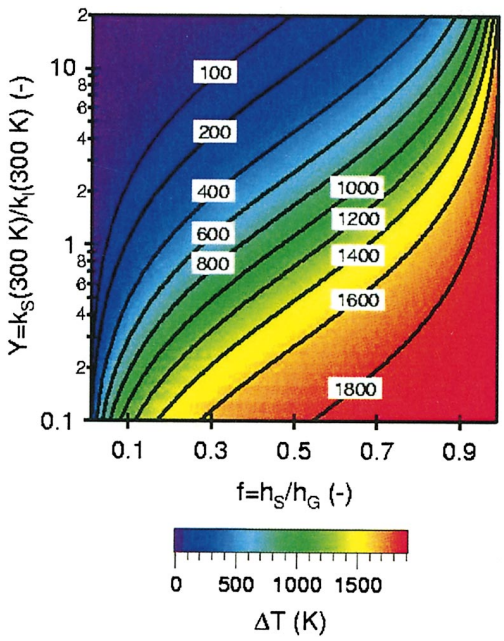

FIG. 6. (Color) The axial temperature drop across the sample as predicted by the one-dimensional analytical model, $\Delta T = T_{max} - T(z = \pm h_S/2)$ and [Eq. (7)] and as a function of the thermal conductivity ratio $Y = k_S/k_I$ and the filling ratio $f = h_S/h_G$ and uniform heating with TEM_{00} mode. T_{max} was fixed at 2200 K.

medium interface can be calculated from the analytical model:

$$\Delta T = T_{max}[1 - \exp(-s)]. \tag{9}$$

A notable feature of Eq. (9) is that the predicted axial temperature drop depends only on the sample filling ratio ($f = h_S/h_G$) and thermal conductivity ratio $[Y = k_S(298\ K)/k_I(298\ K)]$. Accordingly, the axial gradient should remain largely unaffected by changing k_S while keeping the thermal conductivity ratio and sample geometry fixed. A contour plot showing how the axial temperature decrease in the sample as a function of thermal conductivity ratio and filling fraction is shown in Fig. 6 based on the analytical model.

The predictions of the model are consistent with our FE calculations. Fixing $Y=10$ and $f=0.5$ (50% sample filling) we obtain an axial temperature drop from the FE calculations of 216 and 207 K for $k_S=0.1$ W/m K and $k_S=100$ W/m K, respectively. These results compare very favorably with the analytical prediction of 200 K (Figs. 5 and 6). Increasing the sample filling to 0.75 leads to axial temperature drops between 493 and 459 K, again in good agreement with $\Delta T = 505$ K as obtained from the analytical model. The comparison of the one-dimensional analytical model and the results from FE modeling shows good agreement up to sample fillings of at least 75% with differences increasing for higher sample filling but they never exceed 3.6% (80 K) of the peak temperature (2200 K). For low sample filling, the radial heat flow is expected to be dominant [Eq. (6)], an effect not considered in the analytical model. The differences at high sample filling are primarily due to the boundary condition that the temperature on the diamond culet is fixed at 298 K. This assumption breaks down at high sample filling, resulting in an interface temperature that is too low in the analytical model. The heating of the same interface also implies a thermal gradient at the diamond interface that is not been constrained in the analytical model. A closer inspection of the thermal gradient shows that the differences across this interface can account for the remaining temperature difference.

If the filling fraction is $f=0.5$, the axial temperature drop across the sample will range from about 1000 K for a thermal conductivity ratio of 1 to a value of 200 K for a conductivity ratio of 10. An axial temperature drop of $\approx$10% can be achieved with a sample filling fraction of 0.5 if $Y \approx 10$, but requires a filling fraction of 0.1 if $Y \approx 1$. Thus, both the filling fraction and the thermal conductivity ratio are critical for minimizing axial thermal gradients in the laser-heated DAC.

The analytical solution also reproduces the nonmonotonic behavior of the axial temperature profile at the center of the sample as described above (Fig. 4). The optimum sample filling (f_{opt}) that minimizes temperature variations close to the center of the sample is reached for $f_{opt} = Y/(2Y-1)$. For $k_S \gg k_I (Y \gg 1)$, it follows that the optimal sample filling is $f \approx 0.5$. As $Y \to 1$ and differences between sample and insulation decrease, f_{opt} shifts towards 1. For $Y<1$ no optimum is expected and the curvature is always minimized for $f=1$. It is noted that the predicted minimum curvature for intermediate sample filling in the presence of an insulating medium has not been observed previously. Panero and Jeanloz (Ref. 38) found a monotonous broadening of the radial temperature profile with sample filling using semianalytical model. One possible explanation for the differences is that Y may be less than 1 in their study, MgO has a very high thermal conductivity of 55 W/m K even at ambient conditions (Ref.

43) and no reversal would be expected according to our analysis. Therefore, the calculations may apply to different regions in parameter space.

It can be shown that our analytical model reduces to the solution given by Manga and Jeanloz (Ref. 24) for a metallic foil sandwiched between two dielectric layers in the limit $k_S \to \infty$ for finite k_I. In this limit $s \to 0$ and the sample becomes isothermal with $T_S = T_{\max}$. In the dielectric layers we have $-4sY \to -2\ln(T_{\max}/T_0)h_S/(h_G - h_S)$, with the identification of $h_G - h_S = 2L$, where L is the thickness of each dielectric layer, the solution in Ref. 24 is recovered.

The effect of reducing the sample absorption length to values as low as $l = 50$ μm was examined. For heating with a TEM_{00} laser mode, the temperature distribution becomes asymmetrical as expected due to variation in absorption along the axial direction. However, temperature differences between the top and the bottom of the sample remain small, less than 100 K. A more detailed analysis shows that the average temperature drop $\Delta T_{\text{ave}} = (2T_{\max} - T_{\text{top,sample}} - T_{\text{bot,sample}})/2$ tracks the temperature drop of the symmetrical case to within 4 K. Therefore, the analytical model remains valid even for short optical absorption length as long as the average axial temperature drop is considered. This finding can be rationalized by considering the functional from of the absorption length: $\exp(-z/l) \approx 1 - z/l + O((z/l)^2)$ which is antisymmetric with respect to the equatorial plane of the DAC. The same conclusion is reached for the volumetrically averaged temperature. Reducing the absorption length from $l = 200$ μm to 50 μm lowers the volumetrically averaged temperature $(\overline{T})$ in a cylinder of diameter 10 μm from 2033 to 2021 K, by only 0.3%.

Experimentally it is difficult to realize a perfectly symmetrical arrangement of the sample with respect to the diamond culets in the axial direction, and some degree of axial displacement is likely to occur. The FE simulations allow us to calculate the effect of an axially displaced sample on the temperature field. As expected, a perfectly symmetrical arrangement leads to the lowest temperature gradients. An increased axial sample shift leads to a more asymmetrical temperature field (Fig. 7) and the total temperature drop increases (decreases) on the side of the sample where the insulation is thinning (thickening). However, as in the case of the reduced absorption length, the effect is self-averaging. As a result, the average temperature as sampled by a 10-μm diameter x-ray is only weakly affected by the exact axial positioning of the sample. For example, changing the insulation thickness from 50% (symmetric) to 10% on one side (such that the sample is 1.5 μm from one of the diamond culets) while maintaining the total insulation thickness lowers the average temperature from 2000 to 1825 K. Therefore, exact positioning of the sample in the center of DAC is of secondary importance and will contribute strongly to the axial temperature gradients only in the cases for which the insulation is very thin (<2 μm).

The simulations reported here apply to optically thin samples. This is most directly applicable to the case of CO_2 laser heating of Fe-free oxides and silicates or Nd: Yttrium aluminum garnet (YAG) or Nd:YLF heating of Fe-bearing silicates and oxides. Other laser-heating experiments use

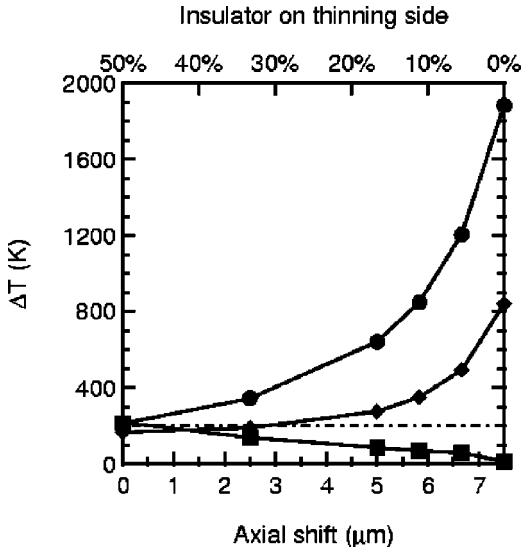

FIG. 7. The effect of axial sample position on the temperature distribution for 50% sample filling and homogeneous heating with the TEM_{00} laser mode. The gasket thickness is fixed at 30 μm Circles, (squares) axial temperature decrease on the thinning (thickening) insulation side. Diamonds: volumetrically averaged sample temperature within a cylindrical volume of a 10-μm diameter. Dot-dashed line: temperature from the symmetrical one-dimensional model. The solids lines are guides to the eye.

Nd:YAG or Nd:YLF layers to heat metallic samples or transparent samples that have been mixed with a laser absorbing medium (typically platinum). In the latter case, uniform absorption throughout the sample length may not apply. However, the amount of laser absorbing medium used in different experiments is quite variable, and our simulations are likely to remain relevant for many of these experiments which often use very small amounts of absorbing medium. In future work, examination of a wider range of sample geometries including those relevant to several different methods of Nd:YAG heating will be reported.

The above discussion also highlights the importance of the thermal conductivity ratio between the sample and the insulator. However, high P-T values of thermal conductivities are generally poorly constrained despite the recent experimental and theoretical advances.[51,56] At very high pressures, conductivity differences among silicates, oxides, and rare gas solids may be greatly diminished, thereby increasing axial temperature gradients. Better understanding of thermal conductivity is needed to better constrain diamond cell temperature gradients.

IV. SUMMARY

Finite element simulations of the temperature field in the laser-heated diamond cell have been used to determine the parameters that control the axial and radial temperature gradients. We have performed simulations for a typical experimental geometry consisting of an optically thin sample separated from the diamond anvils by an insulation medium of varying thickness and heated using the Gaussian (TEM_{00}) mode from an infrared laser. Simulations were carried out for a peak sample temperature of 2200 K. Temperatures on the diamond culet remain close to ambient temperature independent of the laser-heating mode and the sample filling.

The axial temperature gradients in the laser-heated diamond-anvil cell are primarily determined by two factors: the sample filling fraction (ratio of sample thickness to gasket thickness) and the ratio of thermal conductivities of sample and insulator, k_S/k_I. The total axial temperature decrease across the sample from our simulations could be closely approximated by a one-dimensional analytical model. Deviations between our model and the FE calculations can be attributed to the neglect of radial heat flow in the one-dimensional model and the unconstrained heat flow across the diamond culet interface.

For $k_S/k_I=10$, the axial temperature drop along the DAC axis is less than 10% when sample filling fractions are 0.5 or less. If the sample filling fraction is 50% but the ratio of thermal conductivies is instead unity, a large axial temperature difference of 1070 K (50%) is found between the center and the edges of the sample. This highlights the importance of large conductivity ratio between the sample and the insulator. Averaged temperatures across an x-ray sampled volume were calculated by integrating over a 10-μm diameter area through the sample.

The use of insulators with high thermal conductivities such as MgO, Al_2O_3, or NaCl is unlikely to prevent the development of substantial axial gradients when heating silicate samples. In contrast we find that the average temperature field in the sample is much less affected by the axial positioning of the sample. Reducing the insulation thickness to 10% on one side for 50% sample filling decreases the average temperature sampled by a 10-μm diameter x-ray beam by only 10% as compared to optimal symmetrical positioning.

Minimization of axial temperature gradients can also be achieved for thin samples (low filling ratio). For a sample filling ratio of $f=0.2$, an axial temperature drop of $\approx$10% can be achieved for a conductivity ratio, k_S/k_I as low as 3. However, small filling ratios may conflict with experimental requirements of thick samples to obtain sufficient x-ray diffraction intensity. On balance, experiments which aim to minimize axial gradients when using optically thin samples need to employ low conductivity insulation media, thin samples and/or thick gaskets.

For a given gasket thickness and using $k_S/k_I=10$, radial temperature gradients obtained from a Gaussian laser input initially decrease as sample filling fraction increases. The radial gradient reaches a maximum value at around 50% filling, and then decrease at higher filling fractions. The total variation of full width at half maximum of the radial temperature distribution is 25% for filling ratios between 10% and 90%.

ACKNOWLEDGMENTS

We wish to thank S. Speziale and W. Panero for helpful discussions. We also thank the reviewer for helpful comments and suggestions. This research was supported by COMPRES, the Consortium for Materials Properties Research in Earth Sciences under NSF Cooperative Agreement Grant No. EAR 01-35554.

[1] L. Ming and W. A. Bassett, Rev. Sci. Instrum. **45**, 1115 (1974).
[2] L. Chudinovskikh and R. Boehler, Nature (London) **411**, 574 (2001).
[3] S.-H. Shim, T. S. Suffy, and G. Y. Shen, Nature (London) **411**, 571 (2001).
[4] L. Chudinovshikh and R. Boehler, Earth Planet. Sci. Lett. **219**, 285 (2004).
[5] A. Zerr and R. Boehler, Science **262**, 553 (1993).
[6] R. Boehler and R. Zerr, Science **264**, 280 (1994).
[7] G. Y. Shen and P. Lazor, J. Geophys. Res. **100**, 17699 (1995).
[8] G. Y. Shen, H. K. Mao, R. J. Hemley, T. S. Duffy, and M. L. Rivers, Geophys. Res. Lett. **25**, 373 (1998).
[9] D. Errandonea, B. Schwager, R. Ditz, C. Gessmann, R. Boehler, and M. Ross, Phys. Rev. B **63**, 132104 (2001).
[10] G. Y. Shen, V. B. Prapapenka, M. L. Rivers, and S. R. Sutton, Phys. Rev. Lett. **92**, 185701 (2004).
[11] S. R. Shieh, T. S. Duffy, and B. S. Li, Phys. Rev. Lett. **89**, 255507 (2002).
[12] M. Murakami, K. Hirose, K. Kawamura, N. Sata, and Y. Osishi, Science **304**, 855 (2004).
[13] S.-H. Shim, T. S. Duffy, R. Jeanloz, and G. Y. Shen, Geophys. Res. Lett. **31**, L10603 (2004).
[14] M. Murakami, K. Hirose, S. Ono, and Y. Ohishi, Geophys. Res. Lett. **30**, 1207 (2003).
[15] O. Tschauner, A. Zerr, S. Specht, A. Rocholl, R. Boehler, and H. Palme, Nature (London) **398**, 604 (1999).
[16] A. Dewaele, G. Fiquet, D. Andrault, and D. Hausermann, J. Geophys. Res. **105**, 2869 (2000).
[17] S.-H. Shim and T. S. Duffy, J. Geophys. Res. **105**, 25955 (2000).
[18] D. L. Heinz and R. Jeanloz, in *High-Pressure Research in Mineral Physics*, edited by M. H. Manghnani and Y. Syono (Terra Scientific, Tokyo, 1987), pp. 113–127.
[19] A. Jephcoat and S. P. Besedin, Philos. Trans. R. Soc. London, Ser. A **354**, 1333 (1996).
[20] R. Boehler, Philos. Trans. R. Soc. London, Ser. A **354**, 1265 (1996).
[21] R. Jeanloz and A. Kavner, Philos. Trans. R. Soc. London, Ser. A **354**, 1279 (1996).
[22] S. Bodea and R. Jeanloz, J. Appl. Phys. **65**, 4688 (1989).
[23] X. Li, M. Manga, J. H. Jeffreys, and R. Jeanloz, Geophys. Res. Lett. **23**, 3775 (1996).
[24] M. Manga and R. Jeanloz, J. Geophys. Res. **102**, 2999 (1997).
[25] M. Manga and R. Jeanloz, in *Properties of Earth and Planetary Materials at High Pressure and Temperature*, Geophysical Monograph Series Vol. 101, edited by M. Manghnani and T. Yagi (American Geophysical Union, Washington, DC, 1998), pp. 17–25.
[26] A. Dewaele, G. Fiquet, and P. Gillet, Rev. Sci. Instrum. **69**, 2421 (1998).
[27] H. Morishima and H. Yusa, J. Appl. Phys. **83**, 4572 (1998).
[28] R. Boehler and A. Chopelas, in *High-Pressure Research: Applications to Earth and Planetary Sciences*, edited by Y. Soyono and M. H. Manghnani (Terra Scientific, Tokyo, 1992), pp. 55–60.
[29] G. T. Zou, H. K. Mao, R. J. Hemley, and S. A. Gramsch, Rev. Sci. Instrum. **72**, 1298 (2001).
[30] H. K. Mao, G. Shen, R. J. Hemley, and T. S. Duffy, in *High-Pressure Reseach: Properties of Earth and Planetary Materials*, edited by M. H. Manghnani and T. Yagi (American Geophysical Union, Washington, DC, 1998), pp. 27–34.
[31] R. Boehler, N. van Bargen, and A. Chopelas, J. Geophys. Res. **95**, 21 (1990).
[32] D. L. Heinz, J. S. Sweeney, and P. Miller, Rev. Sci. Instrum. **62**, 62 (1991).
[33] G. Y. Shen, M. L. Rivers, Y. Wang, and S. R. Sutton, Rev. Sci. Instrum. **72**, 1273 (2001).
[34] C. Meade, H. K. Mao, and J. Z. Hu, Science **268**, 1743 (1995).
[35] K. Brister and W. A. Bassett, Rev. Sci. Instrum. **66**, 2698 (1995).
[36] D. Andrault and G. Fiquet, Rev. Sci. Instrum. **72**, 1283 (2001).
[37] T. Yagi, T. Kondo, T. Watanuki, O. Shimomura, and T. Kikegawa, Rev. Sci. Instrum. **72**, 1293 (2001).
[38] W. Panero and R. Jeanloz, J. Geophys. Res. **106**, 6493 (2001).
[39] W. Panero and R. Jeanloz, Rev. Sci. Instrum. **72**, 1306 (2001).
[40] W. Panero and R. Jeanloz, J. Appl. Phys. **91**, 2769 (2002).
[41] Y. Fukao, H. Mizutani, and S. Uyeda, Phys. Earth Planet. Inter. **1**, 57 (1968).
[42] A. S. Marfunin, *Physics of Minerals and Inorganic Materials* (Springer, New York, 1979).
[43] A. M. Hofmeister, Science **283**, 1699 (1999).
[44] C. Clauser and E. Huenges, in *Rock Physics and Phase Relations*, edited

by T. J. Ahrens (American Geophysical Union, Washington, DC, 1995), pp. 105–126.
[45]G. A. Slack, Phys. Rev. **126**, 427 (1962).
[46]S. Andersson and G. Backstrom, Rev. Sci. Instrum. **57**, 1633 (1986).
[47]S. K. Saxena, G. Shen, and P. Lazor, Science **264**, 405 (1994).
[48]M. Isshiki *et al.*, Nature (London) **427**, 60 (2004).
[49]I. N. Krupskii and V. G. Manzhelii, Sov. Phys. JETP **28**, 1097 (1969).
[50]F. Clayton and D. N. Batchelder, J. Phys. C **6**, 1213 (1973).
[51]K. V. Tretiakov and A. Scandolo, J. Chem. Phys. **120**, 3765 (2004).
[52]A. P. Jephcoat, Nature (London) **393**, 355 (1998).
[53]K. V. Tretiakov and S. Scandolo, J. Chem. Phys. **121**, 11177 (2004).
[54]G. A. Slack, Solid State Phys. **34**, 1 (1979).
[55]Y. L. Orlov, *The Mineralogy of Diamond* (Wiley, New York, 1977).
[56]Y. Xu, T. J. Shankland, S. Linhardt, D. C. Rubie, F. Langenhorst, and K. Klasinski, Phys. Earth Planet. Inter. **143–144**, 321 (2004).